ADVANCED FUNCTIONAL MATERIALS
www.afm-journal.de

Boosting Tumor Apoptosis and Ferroptosis with Multienzyme Mimetic Au Single-Atom Nanozymes Engaged in Cascade Catalysis

Ziyi Wang, Runan Chen, Wenying Zhang, Pengchao Sun, Nan Zhang,* and Yongxing Zhao**

Nanozyme-based catalytic therapy has garnered much attention in cancer treatment for converting endogenous substrates into reactive oxygen species (ROS), which induce oxidative stress damage in tumors. However, the effectiveness of nanozymes is hindered by the limited availability of these endogenous substrates in the tumor microenvironment. To address this, a novel gold-based single-atom nanozyme (AuSAN), glucose oxidase (GOx, G), and lactate oxidase (LOx, L) are meticulously engineered into a highly ordered biomimetic composite nanozyme M/GLB@AuSAN, forming an interconnected cascade catalysis that catalyzes the carbon sources of tumor into ROS as a sustained antitumor strategy. The loaded GOx and LOx aerobically catalyze glucose and lactate to produce H_2O_2, which is then rapidly converted into ·OH, $O_2^{\bullet-}$, and O_2 by AuSAN. The generated O_2 serves as a positive feedback substrate for further GOx- and LOx-mediated aerobic catalysis, significantly amplifying cascade catalysis, and thereby enhancing ROS accumulation. The abundant intracellular ROS and scarce carbon sources effectively exacerbate protein phosphorylation, lipid peroxidation, and mitochondrial damage, ultimately provoking tumor apoptosis and ferroptosis in vitro and in vivo. Therefore, the integrated design of GOx/LOx/AuSAN provides a promising strategy to combine multiple enzymatic activities, deplete carbon sources, and enhance ROS production, resulting in the suppression of melanoma progression.

1. Introduction

In recent years, nanocatalytic medicine has driven significant advances in innovative biomedical solutions, which trigger specific catalytic reactions within the specific physiological environment, converting non-toxic or less toxic substrates into effective therapeutic products in situ.[1] This approach holds promise for cancer treatments by leveraging H_2O_2 and O_2 presented in the tumor microenvironment (TME) to generate cytotoxic reactive oxygen species (ROS) (such as ·OH, $O_2^{\bullet-}$, and $^1O_2$), which attack the DNA, proteins, and lipids to induce regulated death of tumor cells.[1b,2] However, the limited availabilities of H_2O_2 (100 μM) and O_2 (7–28 mm Hg) in the TME diminish the efficacy of these therapies over time.[3] Once H_2O_2 and O_2 are rapidly depleted by nanocatalysts, it may suppress or minimize the chemical dynamic therapies.[4] Therefore, it is crucial to develop methods for generating H_2O_2 and O_2 in situ within the TME to ensure the sustainability and efficacy of nanocatalysts.

To address the substrate scarcity of nanocatalysts in tumor treatment, cascade catalysis offers a promising solution.[5] It involves a series of reactions where the product of each reaction becomes the substrate for the next catalytic step, thereby efficiently converting the starting substrate into the desired product.[6] Expanding on this concept, the high throughput exchange of glucose and lactate between tumor cells and TME can provide abundant substrates for the in situ generation of H_2O_2.[7] Key enzymes in this approach include glucose oxidase (GOx, G) and lactate oxidase (LOx, L). GOx catalyzes the oxidation of glucose (a kind of cellular carbon source) into gluconic acid and H_2O_2, while LOx catalyzes the oxidation of lactate (another kind of cellular carbon source) into pyruvic acid and H_2O_2. An innovative approach such as copper sulfide nanozyme (CuS) and GOx based aissolvable polymeric microneedles have integrated enzyme and nanozyme, which has oxidized glucose via GOx to supply H_2O_2 for CuS, further exacerbating the production of lethal ROS by CuS to kill tumor cells.[8] Similarly, LOx-loaded tannic acid (TA)-Fe(III) nanoparticles (NPs) have enabled intracellular

Z. Wang, R. Chen, W. Zhang, P. Sun, N. Zhang, Y. Zhao
School of Pharmaceutical Sciences
State Key Laboratory of Esophageal Cancer Prevention and Treatment
Zhengzhou University
Zhengzhou 450001, P. R. China
E-mail: Pengchao_Sun@zzu.edu.cn; nanzhang@zzu.edu.cn; zhaoyx@zzu.edu.cn
P. Sun, N. Zhang, Y. Zhao
Henan Key Laboratory of Nanomedicine for Targeting Diagnosis and Treatment
Zhengzhou 450001, P. R. China
P. Sun, N. Zhang, Y. Zhao
Key Laboratory of Advanced Drug Preparation Technologies
Ministry of Education of China
Zhengzhou University
Zhengzhou 450001, P. R. China

The ORCID identification number(s) for the author(s) of this article can be found under https://doi.org/10.1002/adfm.202412767

DOI: 10.1002/adfm.202412767

ROS generation by oxidizing lactate in the TME to supply H_2O_2 in situ, followed by TA-Fe(III) NPs transforming H_2O_2 into toxic ·OH radicals.[9] However, the enzymatic activities of GOx and LOx are challenging to sustain in the TME due to O_2 depletion. Adapting to tumor hypoxia, GOx loaded on MnO_2 depletes glucose to generate H_2O_2 into O_2 to further boost H_2O_2 generation and glucose starvation.[10] These strategies involve enzyme/nanozyme cascade catalysis, where natural enzymes prioritize in situ H_2O_2 generation.[8–10] However, the insufficient and single enzyme-like activity of nanozymes often restrict their ability to achieve both ROS formation and O_2 supply to GOx/LOx simultaneously. Therefore, integrating multiple enzyme-mimicking activities into nanozymes is crucial for providing innovative and effective solutions in cascade catalysis.

In recent years, single-atom nanozymes (SANs) have garnered significant interest due to their exceptional catalytic properties and abilities to mimic multiple enzymes.[1b,11] Previous studies have demonstrated that SANs form active centers through the covalent binding of metal atoms with coordinating atoms, which enhances their catalytic capabilities by providing additional electrons.[12] Compared to conventional nanocatalysts, SANs demonstrate superior enzyme-like activities, typically exhibiting better substrate affinities and faster catalytic rates.[13] Another significant advantage is their strong oxidative capability, which endows them with catalase (CAT)-, peroxidase (POD)-, and oxidase (OXD)-like activities.[2] This enables them to specifically and simultaneously catalyze the substrates involving H_2O_2, O_2, and others to generate O_2 and free radicals.[2] When SANs are combined with GOx and LOx in cascade catalysis, H_2O_2 aerobically catalyzed by GOx and LOx would be promptly converted into ·OH, $O_2^{\bullet-}$, and O_2 immediately by SANs. The generated O_2 by SANs serves as the substrate for GOx- and LOx-mediated aerobic catalysis, further increasing the production of ·OH and $O_2^{\bullet-}$. Thus, composite nanozymes assembled from GOx, LOx, and SANs are expected to exhibit efficient catalytic conversion efficiency, significant catalytic amplification, and excellent dual carbon source consumption, but very few studies have been conducted on this topic.

Additionally, the development of novel SANs is an important research area for advancing catalytic therapy, aiming to use fewer precious metals to generate more active sites, thereby reducing manufacturing costs. Au holds high potential in serving as an efficient active center of SANs because of its abundant orbital electrons, which can facilitate catalytic reactions.[12a,14] While Au clusters or nanoparticles in the size range of 0.5–5 nm have shown excellent biocatalytic effects, atomically sized Au may exhibit even stronger active catalytic activities because of its superior electronic structure.[15] Existing researches on atomically Au have highlighted its outstanding performance in catalyzing the acetylene hydrochlorination reaction and enhancing the electrocatalysis efficiency, suggesting that Au coordination active sites significantly enhance the reaction kinetics and catalytic tolerance.[16] Additionally, atomic Au as anchoring sites has participated in the delivery of sulfhydryl-functionalized molecules.[17] Nonetheless, the enzyme-like activities and biological effects of Au single-atom sites remain ambiguous.[18]

Based on these backgrounds, we introduce an efficient cascade catalytic strategy for tumor treatment by utilizing a novel atomically Au-based nanozyme-driven cascade catalytic composite nanozyme system with O_2 participating in positive feedback (**Scheme 1**). Initially, AuSAN with an ultralow metal content was synthesized by introducing Au into a metal-organic framework followed by pyrolysis. The obtained AuSAN exhibited multienzyme mimetic activities, such as POD, OXD and CAT, efficiently degrading H_2O_2 and yielding ·OH, $O_2^{\bullet-}$, and O_2. Subsequently, GOx (G), LOx (L), bovine serum albumin (BSA, B), and AuSAN were integrated to prepare the cascade catalytic system GLB@AuSAN. In this system, GOx and LOx accelerated glucose and lactate consumption, while AuSAN efficiently catalyzed H_2O_2 conversion into ·OH, $O_2^{\bullet-}$, and O_2. Following, the cell membranes extracted from murine B16 melanoma cells (B16-CM, M) were encapsulated on the surface of GLB@AuSAN to leverage the natural affinity of B16-CM for homologous B16 cells, thereby forming M/GLB@AuSAN and enhancing its biocompatibility and cellular uptake. M/GLB@AuSAN selectively catalyzed glucose and lactate, significantly increasing intracellular ROS. This process induced apoptosis and ferroptosis in tumor cells through interlinked cell signaling pathways. Moreover, in vivo studies demonstrated that M/GLB@AuSAN suppressed melanoma proliferation and prolonged the survival time of melanoma-bearing mice, achieving sustained nanocatalytic therapy. Overall, this cascade catalytic composite nanozyme system showcases a promising approach to enhancing the efficacy and sustainability of antitumor treatments. The integration of multienzyme and multienzyme mimetic activities not only prevents substrate depletion but also amplifies catalytic effects, providing an efficient and sustained strategy for anti-melanoma. This study sets a new paradigm for the design and application of advanced nanozyme-based therapeutics.

2. Results and Discussion

2.1. Preparation and Structural Characterization of AuSAN

The preparation of AuSAN involved a four-step approach designed to maximize the utilization of Au atoms and ensure the full exposure of metal sites (Scheme 1).[19] Initially, ZIF-8 was synthesized by the assembly of 2-methylimidazole and $Zn(NO_3)_2{\cdot}6H_2O$. Next, Au^{3+} was physically adsorbed onto the surface of ZIF-8 to obtain Au@ZIF-8.[20] Subsequently, a SiOx shell was deposited on the surface of Au@ZIF-8 via the hydrolysis of tetraethoxysilane under alkaline to produce Au@ZIF-8@SiOx (Figure S1, Supporting Information). It was crucial in preventing the aggregation of Au during the subsequent pyrolysis.[21] Finally, Au@ZIF-8@SiO_x was pyrolyzed at 1000 °C, allowing Zn to evaporate while Au coordinated with surrounding atoms to form active centers.[22] After the removal of the SiO_x shell and possible metal nanoparticles, the nanoparticles were collected and purified with water to obtain AuSAN. The transmission electron microscopy (TEM) image of AuSAN revealed a rhombic dodecahedron morphology with a porous surface and rough contours (**Figure 1A**). N_2 adsorption-desorption analysis demonstrated that both AuSAN and nitrogen-doped carbon carrier (ZIF-CN) possessed large specific surface areas and abundant mesopores, which were advantageous for the adsorption of sufficient substrates and highly efficient drug loading (Figure S2 and Table S1, Supporting Information).[22,23] Energy-dispersive spectroscopy analysis revealed a uniform distribution

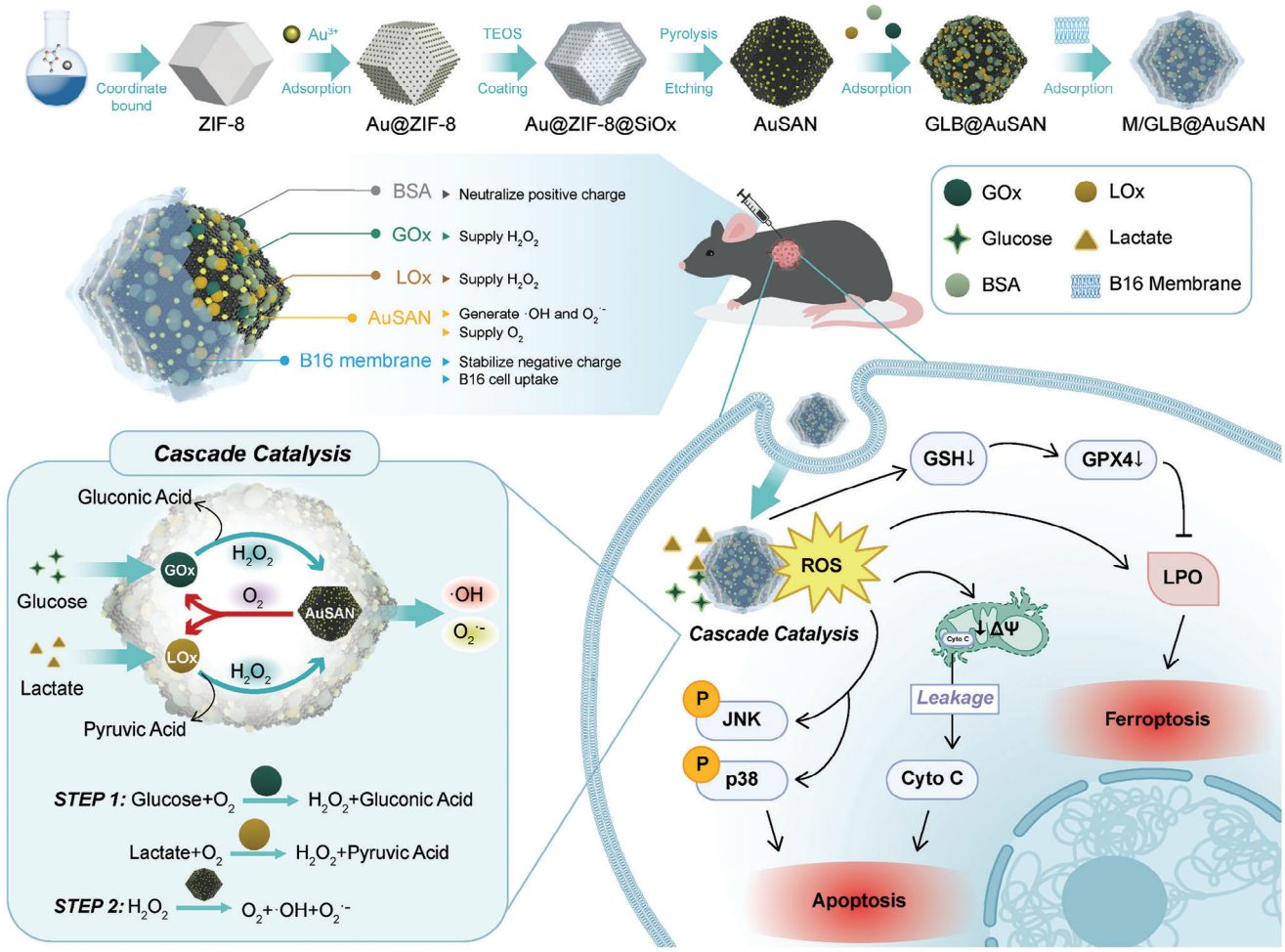

Scheme 1. Schematic illustration of the preparation of M/GLB@AuSAN and the anti-melanoma mechanisms of cascade catalytic therapy.

of C, N, O, and Au atoms throughout AuSAN, signifying the successful integration of Au element (Figure 1D). Inductively coupled plasma-optical emission spectrometry measurement determined the content of Au to be as low as 0.052% (w/w). Crystallographic patterns or lattices were hardly observed by selected area electron diffraction (SAED) and high-resolution TEM in AuSAN (Figure S3, Supporting Information). Likewise, the X-ray diffraction (XRD) pattern of AuSAN excluded the presence of Au crystal (ICDD: 00-001-1174) (Figure 1L and S4, Supporting Information), implying that Au was highly dispersed on the support. The XRD pattern of AuSAN displayed two peaks at 25° and 43°, corresponding to the (002) and (101) planes of graphite, respectively (Figure 1L).[24] Raman spectrum of AuSAN peaked at 1340 cm^{-1} (D band, defect-induced) and 1588 cm^{-1} (G band, sp^2 carbon), which confirmed the amorphous structure of the carbon species (Figure 1M). Notably, the I_D/I_G ratio of AuSAN was slightly higher than that of ZIF-CN, indicating an increase in carbon defect sites due to Au doping (Table S2, Supporting Information).[25] These results primarily confirmed the successful preparation of AuSAN. Subsequently, the distribution status of Au was further investigated through spherical aberration-corrected high-angle annular dark-field scanning transmission electron microscopy (ac-HAADF-STEM) and synchrotron radiation to verify the fine structure of AuSAN. As shown in Figure 1B,C, individual bright spots (highlighted by yellow circles) from the scattering of Au atoms were clearly observed with highly dense, confirming the presence of isolated Au atoms. These results suggested that the limited Au atoms (0.052%) were likely anchored on the surface of AuSAN and served as effective catalytic sites.[26] To further elucidate the status and coordination environment of Au in AuSAN, X-ray absorption fine structure (XAFS) spectroscopy was applied.[27] As seen in Figure 1E, both AuSAN and Au_2O_3 displayed white line peaks (≈11924 eV) at the Au L_3 edge, which was attributed to electron transitions from the 2p to the 5d orbital.[16a] In contrast, Au foil lacked such peaks due to the nearly complete filling of its 5d states.[16a] The intensity of the white line peak for Au in the AuSAN suggested that the valency of Au was between 0 and + 3.[28] Subsequently, Fourier transform extended XAFS (FT-EXAFS) revealed a prominent peak (≈1.6 Å) in the R-space of AuSAN, with the absence of Au-Au contributions (≈2.5 and 2.9 Å) (Figure 1F). Furthermore, wavelet transforms EXAFS (WT-EXAFS) distinguished the Au-N(O) scattering (≈4.0 $Å^{-1}$) in AuSAN from the Au-O scattering (≈4.4 $Å^{-1}$) in Au_2O_3, both of which differed significantly from the

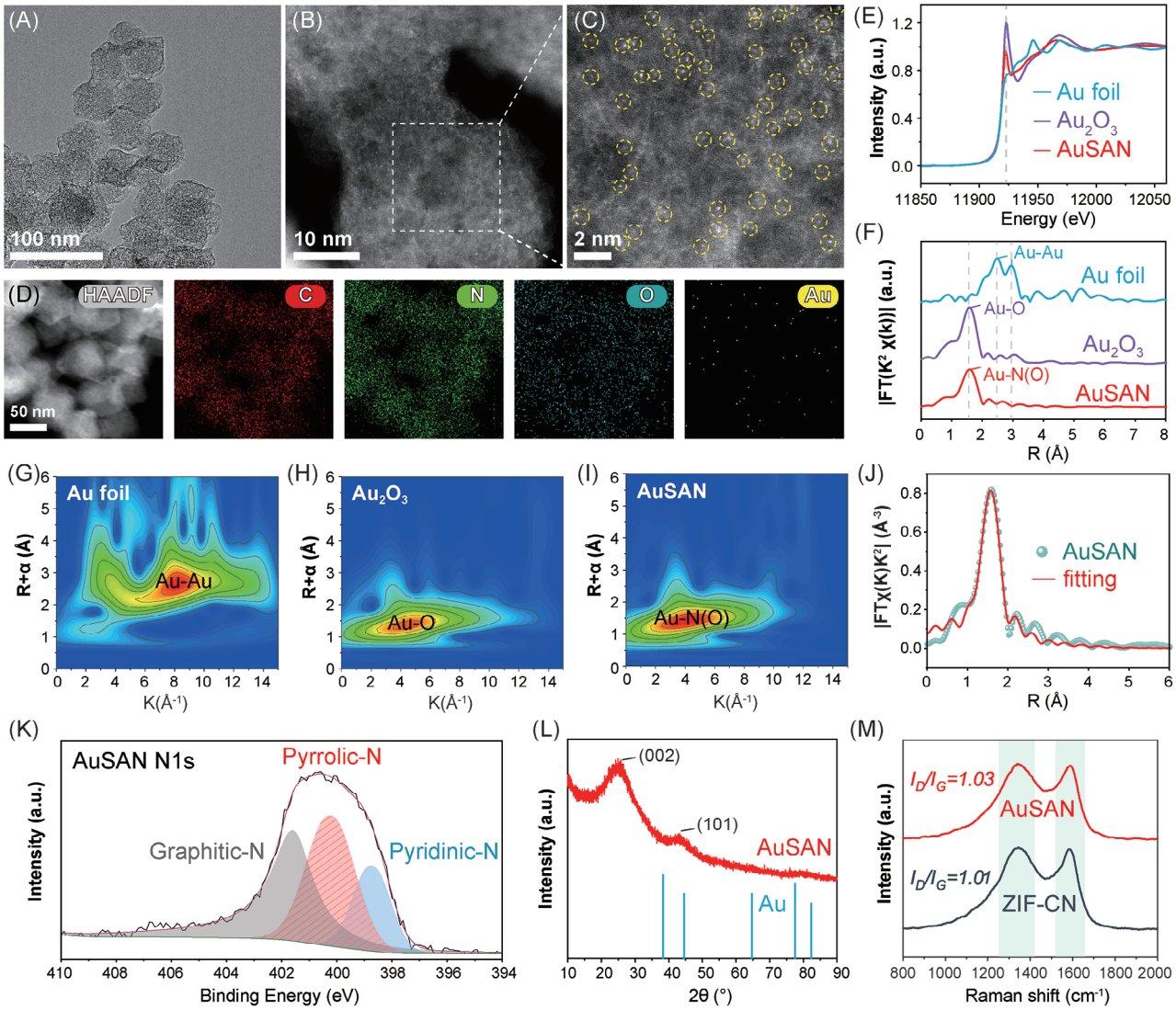

Figure 1. Characterization of AuSAN. A) TEM image of the AuSAN. B) Ac-HAADF-STEM images and C, highlighted by yellow circles) the single atomic Au sites in the AuSAN sample. D) HAADF image of AuSAN and the corresponding elementary mapping. E) Au L_3-edge normalized X-ray absorption near edge structure spectra. F) FT-EXAFS spectra at the Au L_3 edge of AuSAN and reference samples. WT-EXAFS plots of G) Au foil, H) Au_2O_3, and I) AuSAN. J) EXAFS fitting curves of AuSAN in R space. K) XPS spectra of N 1s for AuSAN. L) XRD patterns of AuSAN and Au. M) Raman spectra of AuSAN and ZIF-CN.

Au-Au scattering (≈8.1 $Å^{-1}$) observed in Au foil (Figure 1G–I). Both FT-EXAFS and WT-EXAFS confirmed the atomic dispersion of Au species in the AuSAN, as initially indicated by ac-HAADF-STEM images. Furthermore, the EXAFS fitting of the structural parameters substantiated the high reliability of the Au–N coordination (Figure 1J). The coordination number of N was determined to be 2.7 ± 0.1 for Au of the AuSAN, which pointed toward the possible presence of Au–N_3 active center (Figure S5 and Table S3, Supporting Information). This active center configuration is crucial for understanding the catalytic activity of AuSAN.

X-ray photoelectron spectroscopy (XPS) was applied to further reveal the information on the ingredients and chemical status of AuSAN. As illustrated in Figure S6 (Supporting Information), the survey scan exposed the presence of C, N, and O in both AuSAN and ZIF-CN. The absence of Au signal in AuSAN was likely attributed to the low content, which was consistent with the previous publications.[29] The fine spectra of N in both AuSAN and ZIF-CN displayed pyrrolic, pyridinic, and graphitic N species (Figure S7, Supporting Information). Compared to ZIF-CN, the pyrrolic N in AuSAN increased from 34.9% to 38.2%, indicating that it was predominantly the pyridinic N that coordinated with Au (Figure 1K; Table S4, Supporting Information)[22,30] Taken together, these comprehensive characterizations demonstrate the successful construction of AuSAN with an ultralow content of Au atoms that were uniformly dispersed on the surface of ZIF-CN. These Au atoms coordinated with the surrounding N elements to form Au–N_3. Besides, AuSAN and ZIF-CN exhibited unsaturated nitrogen species (pyrrolic and pyridinic N) and carbon defects, which were beneficial for promoting

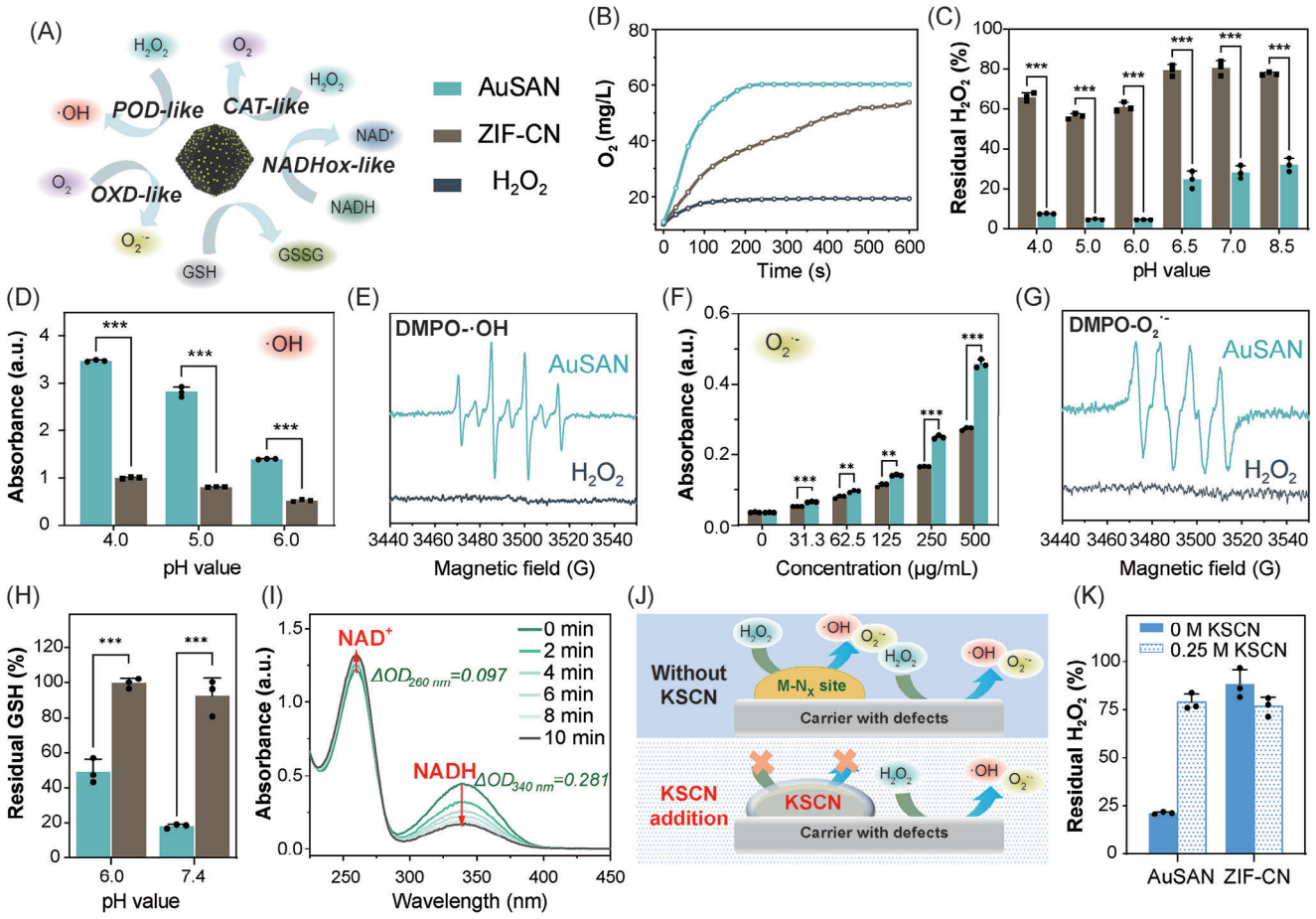

Figure 2. Enzyme-like performance of AuSAN. A) Schematic illustration of the multienzyme mimetic activities of AuSAN. B) O_2 production profiles in the presence of nanozymes (50 μg mL^{-1}) and H_2O_2 (10 mM) at 37 °C ($n = 3$). C) ZIF-CN and AuSAN (100 μg mL^{-1}) induced H_2O_2 degradation at different pH values ($n = 3$). ZIF-CN and AuSAN (100 μg mL^{-1}) catalyzed ·OH generation, examined by D) TMB (1 mM) ($n = 3$) and E) EPR spectroscopy. ZIF-CN and AuSAN (0, 31.3, 62.5, 125, 250, and 500 μg mL^{-1}) catalyzed $O_2^{\bullet-}$ generation, indicated by F) TMB (1 mM) ($n = 3$) and G) EPR spectroscopy. H) The influences of ZIF-CN and AuSAN (30 μg mL^{-1}) on GSH levels at different pH conditions ($n = 3$). I) UV–Vis spectra of the mixture after incubation of NADH with AuSAN for different time periods ($n = 3$). J) Schematic illustration of KSCN poisoning experiment. K) The influence of AuSAN on H_2O_2 levels with/without the presence of KSCN ($n = 3$). $^{**}p \leq 0.01$, $^{***}p \leq 0.001$.

interaction with the substrate.[23a] The designed AuSAN was expected to exert outstanding catalytic performances by maximizing the utilization of the active sites and facilitating substrate binding.

2.2. Catalytic Performances of AuSAN

AuSAN features typical metal-Nx sites and the enhanced local electronic configuration of Au-N_3 coordination might confer upon AuSAN multienzyme mimetic activities.[12a] Our subsequent investigations focused on the CAT-, POD-, OXD-, and nicotinamide adenine dinucleotide oxidase (NADHox)-like activities of AuSAN (**Figure 2A**).

As demonstrated in Figure 2B,C, both AuSAN and ZIF-CN degraded H_2O_2 and catalyzed the generation of O_2. Whereas AuSAN induced a greater release of O_2 from H_2O_2 compared to ZIF-CN, demonstrating that the CAT-like activity of AuSAN was superior to that of ZIF-CN. Furthermore, AuSAN maintained CAT-like activity across a wide pH range (4.0-8.5), indicating its robustness and potential applicability under diverse environmental conditions (Figure 2C; Figure S8, Supporting Information).

The POD-like activity of a nanozyme enables it to deplete H_2O_2 and generate ·OH (Figure 2A). A typical probe, 3,3′,5,5′-tetramethylbenzidine (TMB), was employed to analyze the production of ·OH. After incubation with H_2O_2, AuSAN catalyzed the oxidation of TMB to generate blue ox-TMB, implying the generation of ·OH. The absorbance of ox-TMB induced by AuSAN was 2.7 to 3.5 times higher than that catalyzed by ZIF-CN in the pH range of 4.0 to 6.0, which highlighted the superior POD-like activity of AuSAN (Figure 2D).[21] The generation of ·OH was further validated using o-phenylenediamine (OPDA) as an indicator. As shown in Figure S9 (Supporting Information), AuSAN facilitated more ·OH generation in a concentration-dependent manner. Additionally, an enzyme kinetics study was conducted with H_2O_2 as the substrate. The maximum reaction rate (V_{max}) for AuSAN was determined to be 1.58×10^{-6} Ms^{-1}, which confirmed the high POD-like catalytic activity to AuSAN (Figure S10A,B,

Supporting Information). The Michaelis constant (K_m) was 9.19 × 10^{-4} M, which was smaller than the other reported SANs, reflecting a higher affinity for H_2O_2 (Figure S10A,B and Table S5, Supporting Information). Subsequently, electron paramagnetic resonance (EPR) spectroscopy was employed to in situ detect the unpaired electrons during the catalytic process. The EPR spectrum of AuSAN displayed the characteristic peaks associated with ·OH, supplying direct evidence for the POD-like activity of AuSAN (Figure 2E).

The OXD-like activity of nanozymes allows for the catalysis of O_2 to produce $O_2^{\bullet-}$, which can subsequently oxidize TMB (Figure 2A). In the presence of O_2, AuSAN efficiently oxidized more TMB than ZIF-CN, demonstrating the superior OXD-like activity of AuSAN (Figure 2F). Moreover, the enzymatic kinetic characteristics of OXD-like activity were investigated by varying the concentration of TMB in the presence of O_2. The high V_{max} (4.26 × 10^{-7} Ms^{-1}) and low K_m (5.67 × 10^{-4} M) of AuSAN indicated its rapid OXD-like catalytic rate and a high affinity to the substrate, comparable to other published SANs (Figure S10C,D and Table S5, Supporting Information). Furthermore, the EPR spectrum of AuSAN displayed characteristic peaks of $O_2^{\bullet-}$ with the presence of H_2O_2, confirming the generation of $O_2^{\bullet-}$ (Figure 2G). Specifically, the catalytic process involved AuSAN first catalyzing the conversion of H_2O_2 into O_2, which was immediately transformed into $O_2^{\bullet-}$ via the OXD-like activity of AuSAN. This sequence of reactions underscored the multifunctional catalytic capabilities of AuSAN, which efficiently mediated both the production of O_2 and subsequent $O_2^{\bullet-}$ generation. GSH plays a critical role in maintaining cellular antioxidant capacity.[31] A thiol indicator, 5,5′-dithiobis (2-nitrobenzoic acid), was employed to detect residual GSH following co-incubation with AuSAN. As depicted in Figure 2H, AuSAN consumed 50.7% and 81.9% of GSH at pH 6 and 7.4, respectively, within 5 min. To further affirm the role of $O_2^{\cdot-}$ in the oxidation of GSH, a GSH solution was purged with nitrogen before the addition of AuSAN. As shown in Figure S11A (Supporting Information), AuSAN colud directly consume GSH, while an increased consumption of GSH was observed when O_2 was present in the reaction system. These results demonstrate that both AuSAN and the in situ generated $O_2^{\cdot-}$ are capable of oxidizing GSH,[32] thereby holding potential in disrupting redox balance and enhancing cellular oxidative stress damage of tumor. In contrast, the GSH consumed by ZIF-CN was negligible. These results implied that AuSAN could oxidize GSH efficiently, which was potentially mediated by Au-N_3 active sites. Additionally, NADH and NAD^+ are essential redox cofactors in metabolism.[33] When incubating NADH with AuSAN or ZIF-CN, the absorbance of the mixture at 340 nm (reduced state of NADH) significantly decreased along with a distinct increase at 260 nm, which corresponded to the oxidized state (NAD^+). This shift confirmed the NADHox-like activity of AuSAN and ZIF-CN (Figure 2I; Figure S11B, Supporting Information). The ability of AuSAN to modulate these essential redox molecules underscores its potential as a versatile catalyst in various biological and chemical applications.

The outstanding activities of AuSAN can be credited to the abundant electron supply provided by Au-N_3 sites, which enhances the efficiency of catalytic reactions.[12a] In order to verify the contribution of Au-N_3 to catalysis, a poisoning experiment was conducted (Figure 2J)[34].The activity of AuSAN diminished significantly after the mental-N_x sites were blocked via KSCN, which confirms that Au-N_3, rather than nitrogen-doped carbon carrier, are the activity centers (Figure 2K). Au-N_3 active centers exhibited remarkable stability and catalytic reproducibility, retaining their effectiveness across a range of conditions, including various pH levels, elevated temperatures, diverse solvents, and multiple reuse cycles (Figure 2C; Figures S12 and S13, Supporting Information).

In summary, AuSAN displayed kinds of enzyme-like activities coupled with impressive catalytic capabilities. Its multifunctional features and robustness under diverse conditions make it an attractive option for further catalytic applications.

2.3. AuSAN-Enhanced Cascade Catalysis Mediated by GLB@AuSAN

Although AuSAN exerted excellent multienzyme mimetic activities to catalyze the generation of ROS, the substrates H_2O_2 and O_2 in the TME were still constrained, potentially hindering its anti-tumor efficacy. To address this issue, GOx and LOx can be integrated to catalyze glucose and lactate in the TME, respectively, thereby enabling in situ generation of H_2O_2 and providing continuous substrate for AuSAN. As shown in **Figure 3A**, a novel composite nanozyme was engineered and defined as GLB@AuSAN by combining GOx, LOx, BSA, and AuSAN, which would reduce the levels of glucose and lactate while amplifying ROS production simultaneously through natural enzymes- and SANs- mediated cascade reactions (Figure 3A,B). Theoretically, the incorporated natural enzymes, GOx and LOx, catalyzed the conversion of glucose and lactate in the TME into H_2O_2, which was an O_2-consuming process. The generated H_2O_2 served as the substrate for AuSAN to boost the production of ROS (·OH and $O_2^{\bullet-}$) as well as O_2 (Figure 3B). The resulting O_2 facilitated the natural enzymes-mediated catalytic process in turn. Additionally, BSA was loaded on the surface through electrostatic and physical adsorption to neutralize the positive charge (Figure 3A; Figure S16, Supporting Information), thereby enhancing the biocompatibility of GLB@AuSAN. With the supernatant depletion method, the loading content of GOx, LOx, and BSA were calculated to be 4.28, 11.43, and 284.26 μg mg^{-1}, respectively.

Further studies were dedicated to examining the cascade catalysis performances of GLB@AuSAN. Composite nanozymes (GLB@AuSAN, GB@AuSAN, and LB@AuSAN) and natural enzymes (GOx+LOx, GOx, and LOx) were incubated with substrate solutions (2 mM glucose and 15 mM lactate in PBS) that mimicked TME at 37 °C. To monitor the ingredients of the mixture during the cascade catalysis process, the concentrations of substrates (glucose, lactate, and O_2), intermediates (H_2O_2), and end products (·OH and $O_2^{\bullet-}$) were quantified (Figure 3C–G). Additionally, AuSAN and B@AuSAN, which lack GOx- and LOx-like activity were set as negative controls. First, the residual glucose and lactate were determined using dinitrosalicylic acid reagent and lactate assay kit, respectively. The composite nanozymes induced a significant decrease in glucose/lactate within 2 h, demonstrating that the loaded GOx/LOx maintained their catalytic activity and led the first catalytic

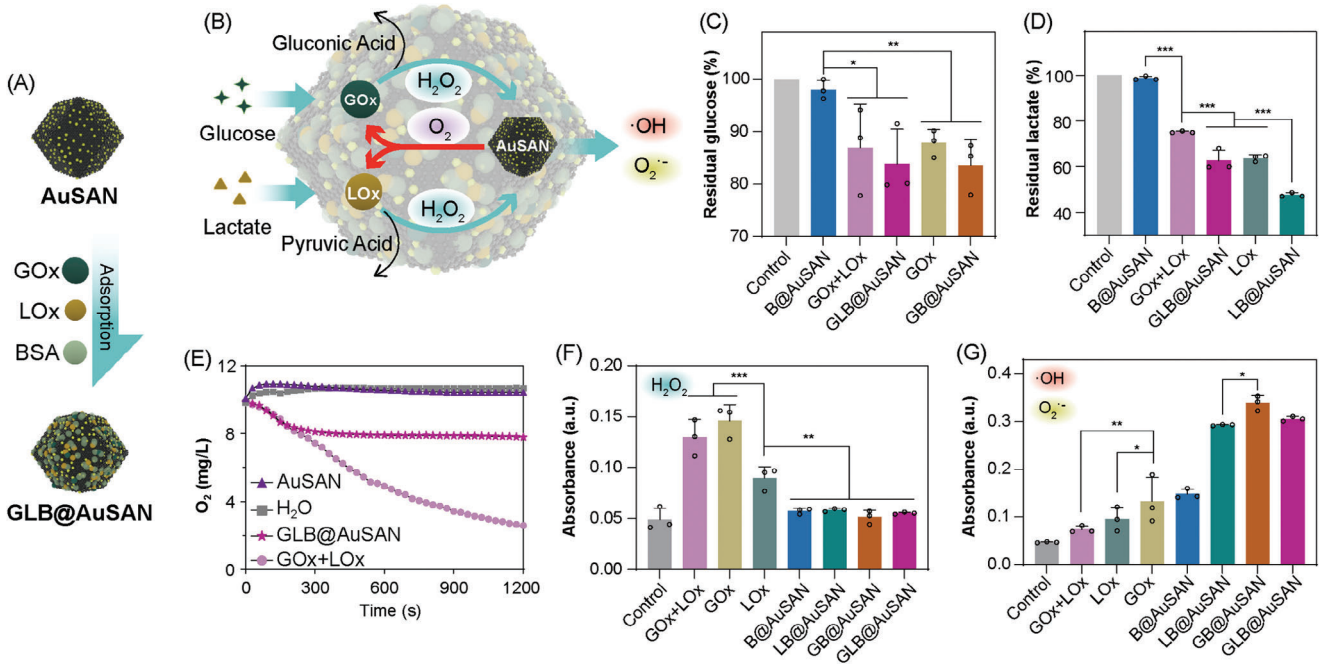

Figure 3. Cascade catalytic performances of GLB@AuSAN. A) Schematic illustration of the fabrication of GLB@AuSAN. B) Schematic illustration of cascade catalysis and O_2-involved positive feedback. The influences of the listed natural enzymes and nanozymes on the consumption of C) glucose and D) lactate, along with the accumulation of F) H_2O_2 and G) ROS after sustained catalysis for 2 h in the presence of glucose (2 mM) and lactate (15 mM) at 37 °C ($n = 3$). E) The corresponding O_2 consumption profiles in the presence of glucose (2 mM) and lactate (15 mM) at 37 °C. *$p \leq 0.05$, **$p \leq 0.01$, ***$p \leq 0.001$.

process of the cascade reactions (Figure 3C,D). Further comparison between composite nanozymes and corresponding natural enzymes (GLB@AuSAN vs GOx+LOx, GB@AuSAN vs GOx, and LB@AuSAN vs LOx) revealed that the immobilized GOx/LOx on the composite nanozymes consumed more glucose within 12 h and/or more lactate within 2 h (Figure S14, Supporting Information; Figure 3D). Moreover, the composite nanozymes alleviated O_2 consumption within 20 min compared to the corresponding natural enzymes (Figure 3E; Figure S15, Supporting Information). This was attributed to the presence of both AuSAN and GOx/LOx in the composite nanozymes, with AuSAN timely compensating for the O_2 consumed in GOx/LOx-mediated catalytic reaction. In addition, no H_2O_2 was accumulated in the TME simulating medium containing the composite nanozymes, implying that H_2O_2 produced by the natural enzymes might promptly be converted into other products (Figure 3F). Next, the TMB chromogenic assay was performed to analyze the generation of free radicals (·OH and $O_2^{\bullet-}$) and verified the second step of the cascade reaction. As depicted in Figure 3G, the absorbance of ox-TMB was relatively low in the TME simulating medium with the presence of natural enzyme alone, indicating that a limited amount of ·OH or $O_2^{\bullet-}$ was produced by the partial auto-oxidation of accumulated H_2O_2 at the test temperature (37 °C).[35] In contrast, B@AuSAN, which lacked GOx and LOx activities, showed an increase in ox-TMB absorbance due to its OXD-like activity. However, the most striking difference was observed in the TME-simulating medium containing the composite nanozymes. The absorbance of ox-TMB was significantly higher, verifying that more ·OH and $O_2^{\bullet-}$ were produced via natural enzymes- and AuSAN-mediated cascade reactions. To summarize, GLB@AuSAN effectively boosted the consumption of both glucose and lactate to generate H_2O_2, which fulfilled the first process of the cascade reaction driven by the natural enzymes. The generated H_2O_2 in situ immediately served as the substrate for AuSAN, initiating the second process of the cascade reaction. The O_2 produced in the second reaction compensated for O_2 consumed in the first process, forming a catalytic loop that accelerated the entire cascade reaction. Consequently, all the complex nanozymes significantly increased the accumulation of ROS during these processes. Despite the potential O_2 competition, which could suppress the activity of GOx and LOx, the dual-enzyme-loaded composite nanozyme still possesses a unique advantage.[36] Specifically, GLB@AuSAN held the potential to simultaneously deplete two cellular carbon sources while maintaining a comparable ROS production performance to GB@AuSAN and LB@AuSAN. This dual functionality enables continuous cascade reactions within TME, integrating ROS production with carbon starvation. Thus, GLB@AuSAN-mediated cascade catalysis emerges as a potent strategy for further anti-melanoma research.

2.4. Characterization, Antitumor Efficacy, and Intracellular Uptake of M/GLB@AuSAN In Vitro

To improve biocompatibility, B16-CM was coated on the surface of the composite nanozyme to obtain a biomimetic composite nanozyme M/GLB@AuSAN via ultrasonication (**Figure 4A**).[37] The resulting M/GLB@AuSAN was well dispersed with a

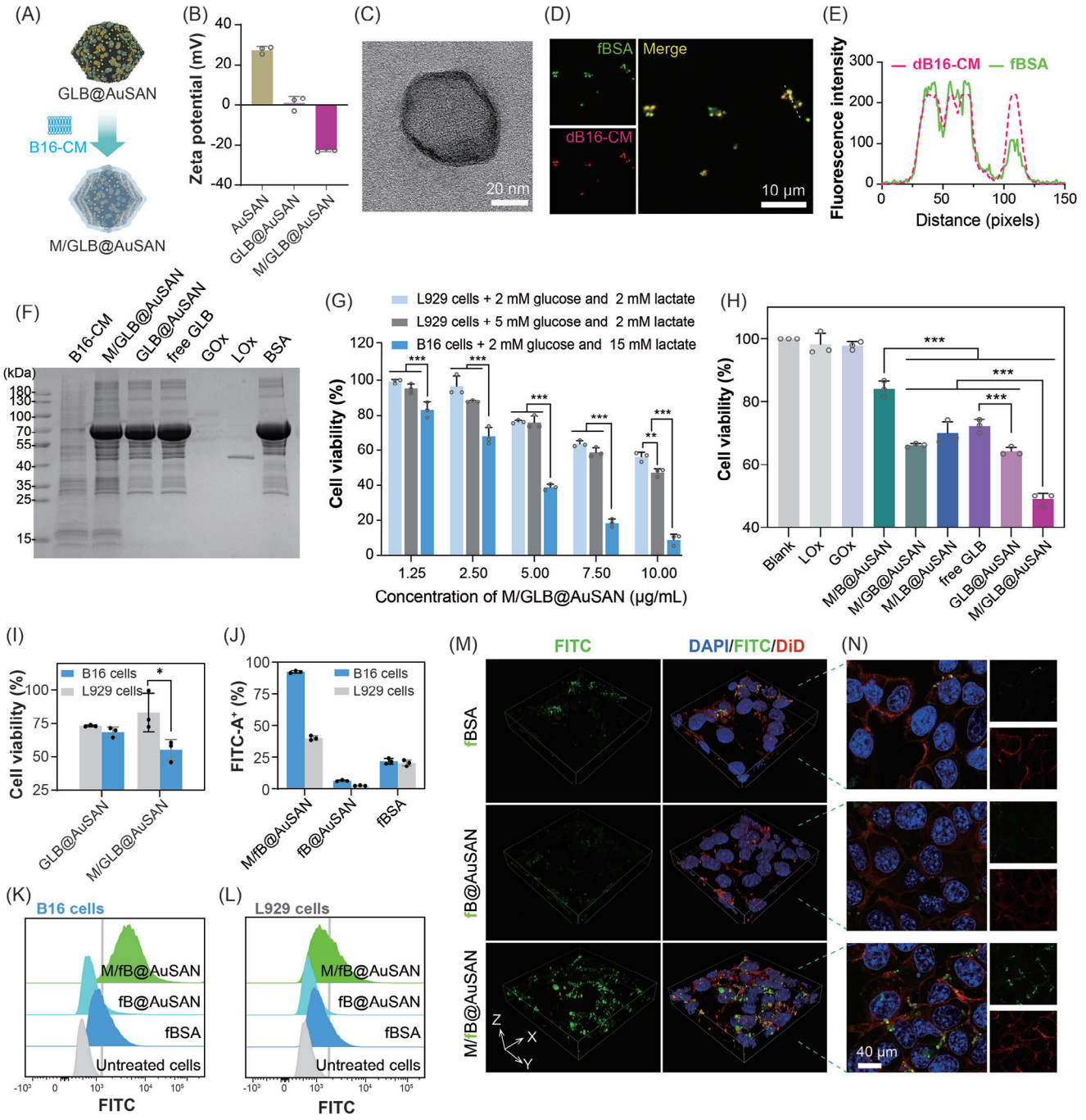

Figure 4. Characterization, antitumor efficacy, and intracellular uptake of M/GLB@AuSAN in vitro. A) Schematic illustration of the fabrication process of M/GLB@AuSAN. B) Zeta potential of AuSAN, M/GLB@AuSAN, and GLB@AuSAN ($n = 3$). C) TEM image of M/GLB@AuSAN. (D) CLSM images of dM/fB@AuSAN fabricated with FITC-labeled BSA (fBSA, green) and DiD-labeled B16-CM (dB16-CM, red). E) Fluorescence intensity at the location of the dotted line derived from D). F) Image of protein bands separated by denaturing polyacrylamide gel electrophoresis. G) Viability of B16 and L929 cells incubated with M/GLB@AuSAN for 12 h in different mediums ($n = 3$). (H) Viability of B16 cells treated with various treatments for 12 h in TME simulating medium (2 mM glucose, 15 mM lactate) ($n = 3$). I) The viability of B16 cells, which was assessed after incubation with various treatments in a glucose-free medium for 4 h and subsequent incubation with TME-mimicking culture medium for 12 h ($n = 3$). Representative flow cytometric plots of K) B16 and L) L929 cells treated with fBSA, fB@AuSAN, and M/fB@AuSAN for 4 h and corresponding J) statistical analysis of FITC-positive cell ($n = 3$). M) 3D image rebuilding and N) sectional views along the z-axis of B16 cells treated with fBSA, fB@AuSAN, and M/fB@AuSAN for 4 h. $^{*}p \leq 0.05$, $^{**}p \leq 0.01$, $^{***}p \leq 0.001$.

negative charge (Figure 4B). TEM further revealed a bilayer structure on the surface of M/GLB@AuSAN, suggesting successful membrane coating (Figure 4C; Figure S17, Supporting Information). SDS-PAGE analysis confirmed the successful integration of GOx, LOx, BSA, and B16-CM within M/GLB@AuSAN (Figure 4F). Subsequently, confocal laser scanning microscopy (CLSM) showed that the fluorescence signal of fluorescein isothiocyanate (FITC)-labeled BSA (green) well matched the signal of 1,1′-dioctadecyl-3,3,3′,3′-tetramethylindodicarbocyanine perchlorate (DiD)-labeled B16-CM (red) with a Pearson product-moment correlation of 0.72, demonstrating the successful integrating of protein and B16-CM on the surface of AuSAN (Figure 4D,E; Figure S18, Supporting Information).[38]

A major objective of M/GLB@AuSAN is to selectively kill melanoma cells in the TME. In a TME simulating condition (2 mM glucose and 15 mM lactate), M/GLB@AuSAN demonstrated dose-dependent inhibition of B16 cell proliferation (Figure 4G). Compared to other strategies, M/GLB@AuSAN exhibited much greater efficacy in killing B16 cells, achieving notable inhibition on B16 cell viability at 5 μg mL^{-1} (Figure 4H). Importantly, under conditions mimicking blood (5 mM glucose and 2 mM lactate) and tissue microenvironments (2 mM glucose and 2 mM lactate), normal L929 fibroblasts maintained high cell viability (Figure 4G). We next tested whether the biomimetic composite nanozyme would have selective cell killing. As shown in Figure 4I, GLB@AuSAN was able to kill B16 cells, but it also exhibited similar cytotoxicity toward L929 cells. However, M/GLB@AuSAN significantly killed B16 cells rather than L929 cells, demonstrating that biomimetic composite nanozymes exhibited selective killing capabilities toward the target cells.

To confirm the correlation between selective cell killing and cellular uptake, FITC-labeled M/fB@AuSAN was used as a model to investigate cell internalization by CLSM and flow cytometry. After 4 h of incubation, M/fB@AuSAN treated B16 cells showed much stronger green fluorescence signals than those cells treated with FITC-labeled BSA (fBSA) and fB@AuSAN (Figure 4M). With the assistance of 3D image rebuilding and sectional images along the z-axis, the green fluorescence signal of M/fB@AuSAN was clearly observed in the cytoplasm with the cell membrane of B16 cells (Figure 4M,N). These findings suggested that M/fB@AuSAN was successfully taken up by B16 cells within 4 h, and B16-CM coating was conducive to cell uptake due to homologous cell recognition.[37] Further quantitative analysis showed that a majority of B16 cells (≈92.3%) were fluorescence positive, which was significantly higher than that of L929 cells (≈39.9%). These findings highlight the significant impact of B16-CM coating on the targeting efficiency of B16 cells (Figure 4J–L).

These evidences supported that M/GLB@AuSAN can selectively kill melanoma cells while maintaining low toxicity to normal cells, demonstrating the potential of M/GLB@AuSAN for effective and safe cancer therapy. Although either GOx or LOx-mediated single carbon source consumption has been integrated with artificial nanozymes for cascade therapy,[39] the simultaneous depletion of both glucose and lactate was beneficial to achieve better anti-tumor activity (Figure 4H). Furthermore, contrary to merely alleviating hypoxia within the tumor microenvironment,[40] the present work highlighted the positive feedback role of O_2, which was essential for amplifying ROS generation (Table S6, Supporting Information).

2.5. Antitumor Mechanism of M/GLB@AuSAN In Vitro

To elucidate the anti-tumor mechanisms in vitro, the occurrence of M/GLB@AuSAN-mediated cascade reactions was explored in the presence of living cells. The concentration of extracellular carbon sources was first determined to investigate the first process of the cascade reactions of M/GLB@AuSAN. Toward this end, substrate-free medium containing biomimetic composite nanozymes and natural enzymes was preincubated with B16 cells for 4 h to ensure that the nanozymes or natural enzymes were taken up by cells. The medium was later replaced with the one mimicking TME and incubated for another 12 h. Subsequently, the residual glucose and lactate levels in the medium as well as cell viability, were quantified. As shown in **Figure 5A**, both natural enzymes and composite nanozymes significantly reduced the extracellular glucose and/or lactate levels. Specifically, M/GLB@AuSAN treated cells showed relatively low levels of extracellular glucose and lactate, along with the lowest cell viability, suggesting a superior capacity to deplete dual carbon sources compared to other groups (Figure 5A,B). These findings verified the successful initiation of the first catalytic process of the cascade reactions.

Further, the intracellular ROS was determined via a ROS probe dichlorodihydrofluorescein (DCFH-DA) to investigate the second process of the cascade reactions that happened in B16 cells. As seen in Figure 5C and Figure S19 (Supporting Information), free GLB (the mixture of GOx, LOx, and BSA) induced modest oxidation of DCFH-DA (2′,7′-dichlorofluorescein, DCF, ≈6.4%) in treated cells, suggesting that natural enzymes generated H_2O_2 by consuming glucose and lactate. In cells treated with M/B@AuSAN, an enhanced signal of DCF (≈62.2%) was observed, highlighting the advantage of AuSAN in elevating intracellular ROS through its multienzyme mimetic activities. Cells treated with M/GB@AuSAN and M/LB@AuSAN exhibited higher DCF signals (≈80.1% and ≈80.4%, respectively), compared to those treated with M/B@AuSAN, demonstrating that cascade catalysis mediated by natural enzymes and AuSAN played a critical role in enhancing ROS accumulation. Most strikingly, GLB@AuSAN and M/GLB@AuSAN showed remarkably high DCF signals (≈86.7% and ≈92.9%, respectively), demonstrating the significant advantage of consuming dual carbon sources through cascade catalysis to induce ROS accumulation. These findings confirmed the successful occurrence of the second catalytic process of the cascade reactions as expected. Based on the aforementioned findings, the high cytotoxicity of M/GLB@AuSAN was highly correlated with carbon starvation and the accumulation of ROS, highlighting the advantages of this cascade catalysis strategy. Upon taken up by B16 cells, M/GLB@AuSAN initiated cascade reactions that depleted intracellular dual-carbon sources. This depletion subsequently prompted these cells to import more glucose and lactate from the extracellular environment, resulting in a significant decrease in extracellular dual carbon sources (Figure 5A).[36] Interestingly, cells treated with GOx and M/GB@AuSAN exhibited not only glucose consumption but also an increase in lactate utilization. A similar phenomenon was observed in cells treated with LOx and M/LB@AuSAN as well. This suggested that the depletion of one substrate intensified the demand for an alternative substrate.[36] In terms of ROS generation, different

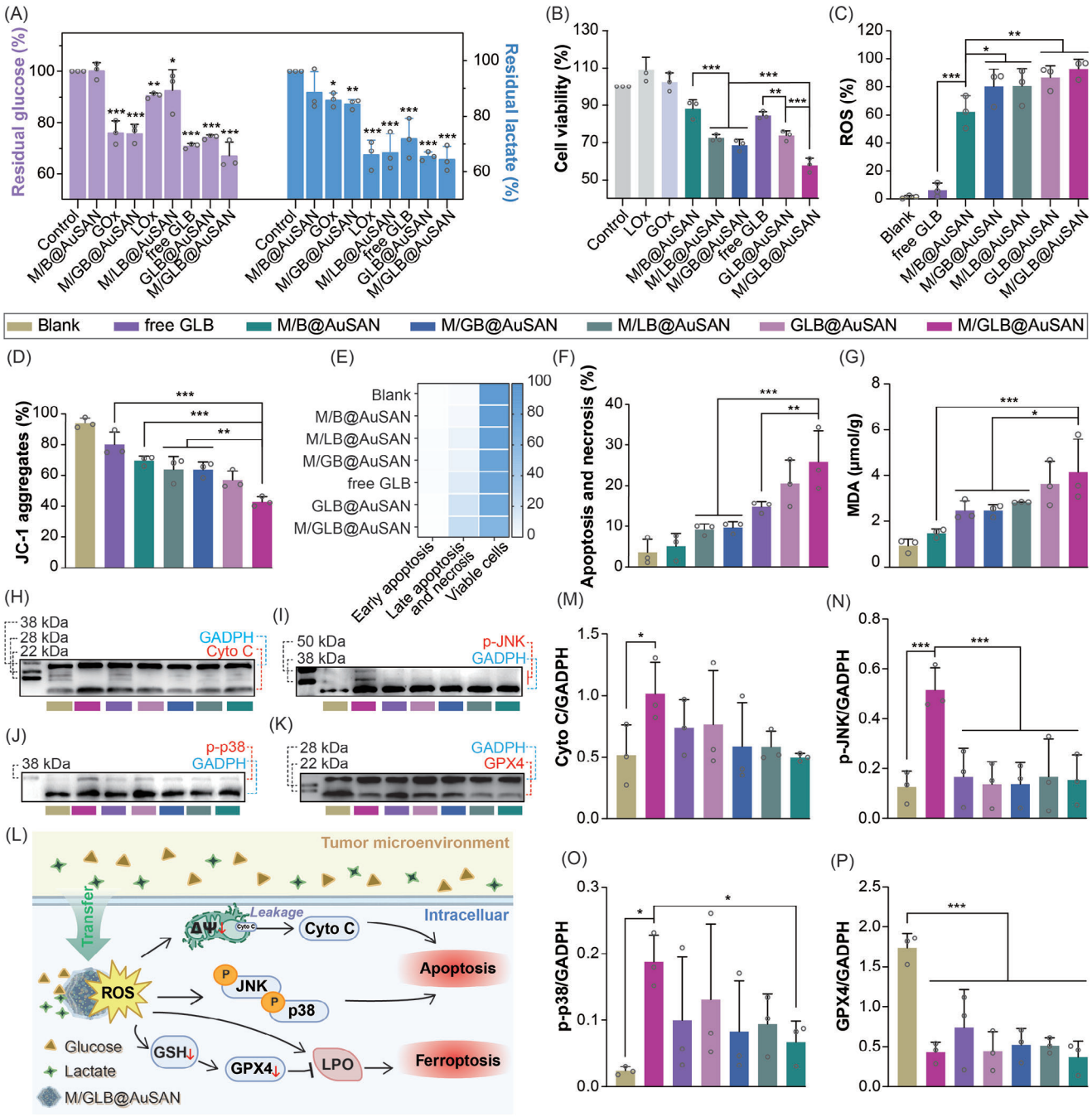

Figure 5. Catalytic performance and potential antitumor mechanism of M/GLB@AuSAN in vitro. A) Residual glucose and lactate in the TME simulating medium and B) corresponding viability of cells ($n = 3$). C) Statistical analysis of ROS-positive B16 cells ($n = 3$). D) Statistical analysis of MMP of B16 cells using JC-1 as a probe ($n = 3$). E) Heatmap of the B16 cell state distinguished using Annexin V-FITC/PI staining and F) corresponding statistical analysis of B16 cell apoptosis and necrosis ($n = 3$). G) Intracellular total MDA levels in B16 cells ($n = 3$). Western blots and corresponding grayscale analysis statistics of (H, M) Cyto C in the cytoplasm lysates and (I, N) p-JNK, (J, O) p-p38, and (K, P) GPX4 in whole-cell lysates ($n = 3$). (L) Schematic illustration of the antitumor mechanism of M/GLB@AuSAN. The heatmap shows the mean values ($n = 3$). $^*p \leq 0.05$, $^{**}p \leq 0.01$, $^{***}p \leq 0.001$.

results were obtained with or without the living cells (Figures 3G and 5C). With the absence of cells, the trend of ROS accumulation was GB@AuSAN > GLB@AuSAN > LB@AuSAN (Figure 3G). However, the intracellular ROS accumulation followed a different trend: M/GLB@AuSAN > M/LB@AuSAN ≈ M/GB@AuSAN (Figure 5C). A proposed explanation for this phenomenon was that cells treated with M/GLB@AuSAN suffered from carbon starvation, which increased the intracellular transport of more carbon sources to support the cascade catalysis.

Excessive intracellular ROS trigger a cascade of detrimental effects, including protein phosphorylation, lipid peroxidation, and organelle damage, which ultimately lead to cell apoptosis

and ferroptosis.[41] Besides, carbon starvation and GSH depletion also increase cell susceptibility to these forms of cell death (Figure 5L).[42] To investigate the extent of mitochondrial damage, the mitochondrial membrane potential (MMP) was first assessed by JC-1 staining. As seen in Figure 5D and Figure S20 (Supporting Information), treatment with M/GLB@AuSAN resulted in decreased fluorescence, thereby indicating the reduction of MMP, which was consistent with the elevated ROS observed in Figure 5C. Western blot analysis further revealed that M/GLB@AuSAN treatment induced a significant release of cytochrome C (Cyto C) from the mitochondria into the cytoplasm, which was probably caused by severe mitochondrial damage (Figure 5H,M).[43] Besides, M/GLB@AuSAN treatment induced the phosphorylation of c-Jun N-terminal kinase (JNK) and p38, indicating the activation of the (mitogen-activated protein kinase (MAPK) signaling pathway (Figure 5I–J,N–O).[41c] Both Cyto C leakage and MAPK activation are known contributors to cell apoptosis.[41c,44] Subsequent analysis using Annexin V-FITC/PI staining confirmed the cell apoptosis (Figure 5E; Figure S21, Supporting Information). The percentages of apoptotic and/or necrotic cells were significantly higher in the M/GLB@AuSAN treatment group than in the other groups, indicating a higher therapeutic efficacy (Figure 5F). Moreover, M/GLB@AuSAN induced substantial malondialdehyde (MDA) accumulation in the treated cells, indicative of lipid peroxidation (LPO) (Figure 5G). The accumulation of LPO could be attributed to ROS accumulation caused by the cascade reactions, which participated in lipid radical chain reactions.[41a] Western blot analysis also revealed that M/GLB@AuSAN inhibited the expression of glutathione peroxidase 4 (GPX4) in the treated cells, possibly by weakening the Xc-/GSH/GPX4 axis through starvation effects and by disrupting GSH via OXD-like activity of AuSAN (Figure 5K,P).[45] The enrichment of LPO and the inhibition of GPX4 led to the collapse of the lipid redox system, which then resulted in ferroptosis.[41a,45] Overall, these studies revealed that M/GLB@AuSAN synergistically induces cell apoptosis and ferroptosis via cascade catalysis.

2.6. Antitumor Efficiency and Mechanism of M/GLB@AuSAN In Vivo

Inspired by the promising tumoricidal effects observed in vitro, we evaluated the antitumor effectiveness of M/GLB@AuSAN in vivo. Taking advantage of the accessibility of melanoma, intratumoral injection (i.t.) was selected as the method for administrating various enzymes/composite nanozymes in vivo. B16-tumor-bearing mice were randomly divided into 8 groups of 6 mice each and administered with M/GLB@AuSAN, M/GB@AuSAN, M/LB@AuSAN, M/B@AuSAN, GLB@AuSAN, or free GLB every two days (**Figure 6**A). The mice that did not receive any treatments and intraperitoneally injected with cisplatin (4 mg kg^{-1}, i.p.) were set as a model and the positive control, respectively.[46] During the observation period (12 days), tumor volumes of the model group mice rapidly increased, indicating swift melanoma progression (Figure 6B; Figure S22, Supporting Information). In contrast, all treatments showed a reduction in tumor size, especially tumors from the M/GLB@AuSAN treated group, which exhibited the smallest tumor volumes, highlighting its remarkable antitumor efficacy. Subsequent inductively coupled plasma-mass spectrometry analysis confirmed that after 12 days of M/GLB@AuSAN treatment, Au was well retained within tumor tissues and with a minimal amount entering the liver and kidneys (Figure S23, Supporting Information). These findings suggested a predominant accumulation of the biomimetic nanozyme system in tumors, with potential hepatic and renal metabolism. Then, administration was stopped and the surval of mice was continuously observed and recorded. As expected, the M/GLB@AuSAN treatment group significantly prolonged the median survival time to 20 days, demonstrating a significant improvement in survival rate (Figure 6C). To assess the efficacy of various treatments in inhibiting tumor growth, the normalized tumor inhibition rate (NTIR) was calculated with M/B@AuSAN serving as the baseline. As shown in Figure 6D, the NTIR values were 12.9% for M/GB@AuSAN and 18.6% for M/LB@AuSAN on the 12th day. Concurrently, dihydroethidium (DHE) staining demonstrated relatively higher fluorescence intensity in tumor tissues post-administration of M/GB@AuSAN (≈31.4%) and M/LB@AuSAN (≈28.8%) than M/B@AuSAN (≈24.9%) (Figure 6E; Figure S24, Supporting Information). This finding indicated that M/GB@AuSAN and M/LB@AuSAN successfully increased tumor ROS and enhanced therapeutic efficacy through the natural enzyme- and AuSAN-mediated cascade catalysis. Notably, the NTIR of the M/GLB@AuSAN group continually increased during the treatment, surpassing that of the M/GB@AuSAN and M/LB@AuSAN groups, and reaching 60.5% at the end of the treatment (Figure 6D). Of particular note, the highest fluorescence intensity was observed in the tumor of the mice administrated with M/GLB@AuSAN (≈36.6%) (Figure 6E; Figure S24, Supporting Information). These results collectively confirmed that M/GLB@AuSAN effectively synergized with dual natural enzymes to supply H_2O_2 for AuSAN, promoted the accumulation of tumor ROS and effectively inhibited tumor proliferation, underscoring the advantages of cascade catalysis. Besides, M/GLB@AuSAN exhibited significantly greater tumor suppression and ROS accumulation capability compared to GLB@AuSAN. Thus enhanced performance is likely attributed to the design of the biomimetic delivery system, which facilitates deeper tumor penetration and improves retention of the composite nanozymes.[47]

Based on the previous findings, histological examination of excised tumor tissues was proceeded to evaluate the induction of apoptosis and ferroptosis. A terminal deoxynucleotidyl transferase dUTP nick end labeling (Tunel) assay showed that M/GLB@AuSAN induced apoptosis in ≈31.2% of the tumor tissue region, which was 52-fold greater than that in the model group (≈0.64%) (Figure 6F; Figure S25A, Supporting Information). Furthermore, immunofluorescence staining revealed a significant reduction in the expression of GPX4 in the M/GLB@AuSAN treatment group to ≈25% of that in the model group, suggesting the occurrence of ferroptosis (Figure 6G; Figure S25B, Supporting Information). Bio-TEM imaging again confirmed M/GLB@AuSAN-induced ferroptosis and apoptosis in melanoma tissues. Untreated tissues exhibited intact cell membranes and nuclei, along with a healthy abundance of organelles such as mitochondria, endoplasmic reticulum, ribosomes, and melanin granules within the cytoplasm (Figure 6H–a,b). In contrast, M/GLB@AuSAN treated group

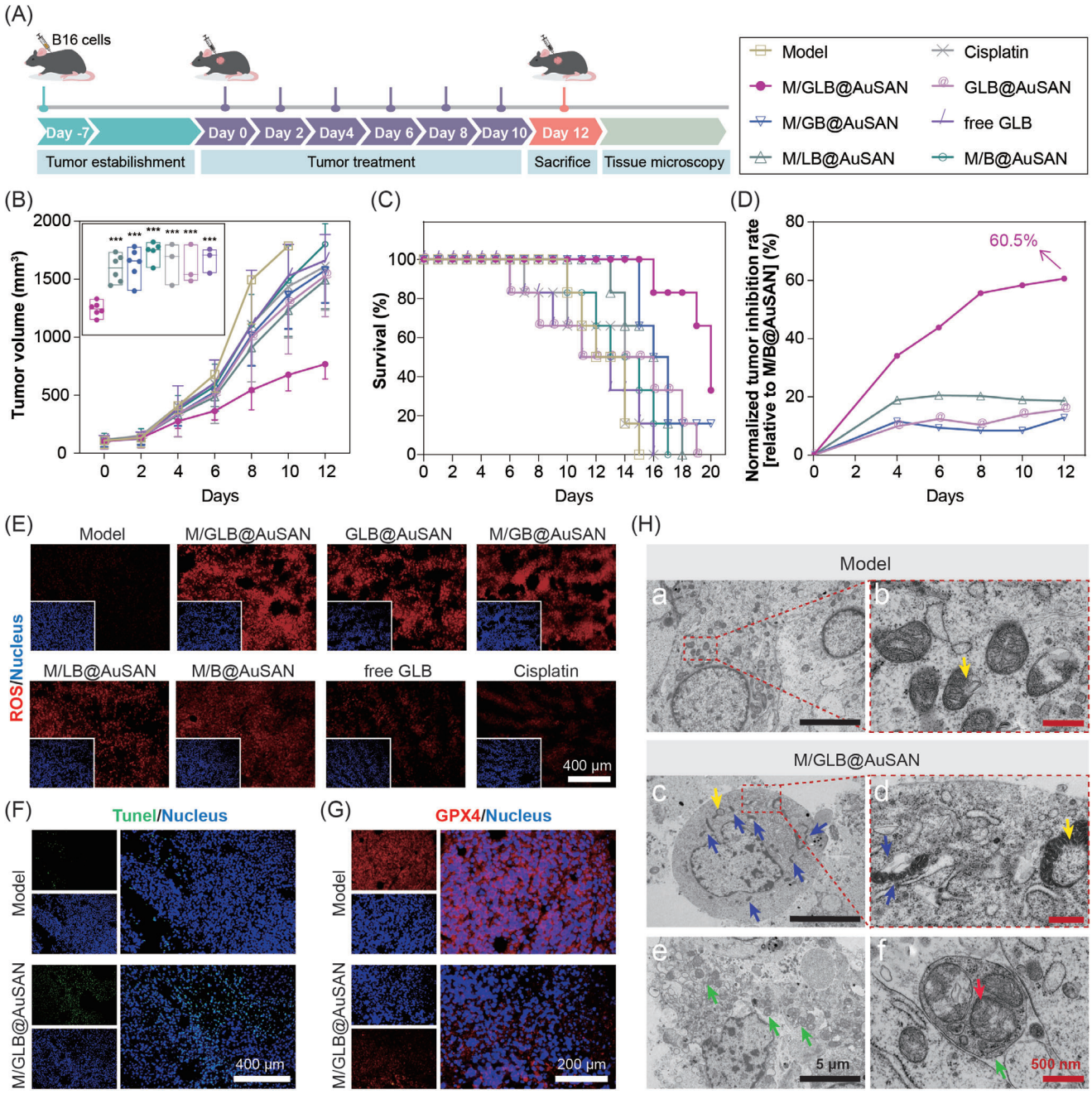

Figure 6. Therapeutic efficacy and antitumor mechanism of M/GLB@AuSAN in vivo. A) Schematic illustration of the in vivo therapeutic process. B) Tumor volume curves under different treatments, with the inset figure showing the tumor volume on the 12th day ($n = 6$). D) Tumor inhibition rates of different treatment groups normalized to the baseline group (M/B@AuSAN). E) Representative images of tumor ROS staining at the endpoint for survival. F) Representative images of Tunel staining and G) GPX4 immunofluorescence assays on the 12th day of the treatment. H) Bio-TEM images of tumors. a and b show melanoma cells and magnified mitochondria from untreated tumor tissue. c, d, e, and f depict melanoma cells treated with M/GLB@AuSAN: c) ferroptosis cell; d) magnified mitochondrial damage; e) apoptotic cell; f) apoptotic body (yellow arrow: mitochondrial autophagy; blue arrow: mitochondrial damage; green arrow: apoptotic body; red arrow: vacuolated mitochondria). ***$p \leq 0.001$.

showed extensive mitochondrial damage, characterized by mitochondrial shrinkage (blue arrows), rupture of the outer and inner membranes (blue arrows), and the occurrence of mitochondrial autophagy (yellow arrows) (Figure 6H–c,d).[41b,48] Interestingly, in contrast to the physiological autophagy observed in Figure 6H–b, mitochondrial autophagy induced by M/GLB@AuSAN treatment occurred in shrunken mitochondria with inner membrane rupture and identified as the typical mitochondrial type III autophagy in response to ferroptosis.[41b,48] These aberrant cellular morphologies were highly consistent with the features of ferroptosis.[41b,48] Additionally, the presence of numerous apoptotic bodies (green arrows) in the M/GLB@AuSAN treated

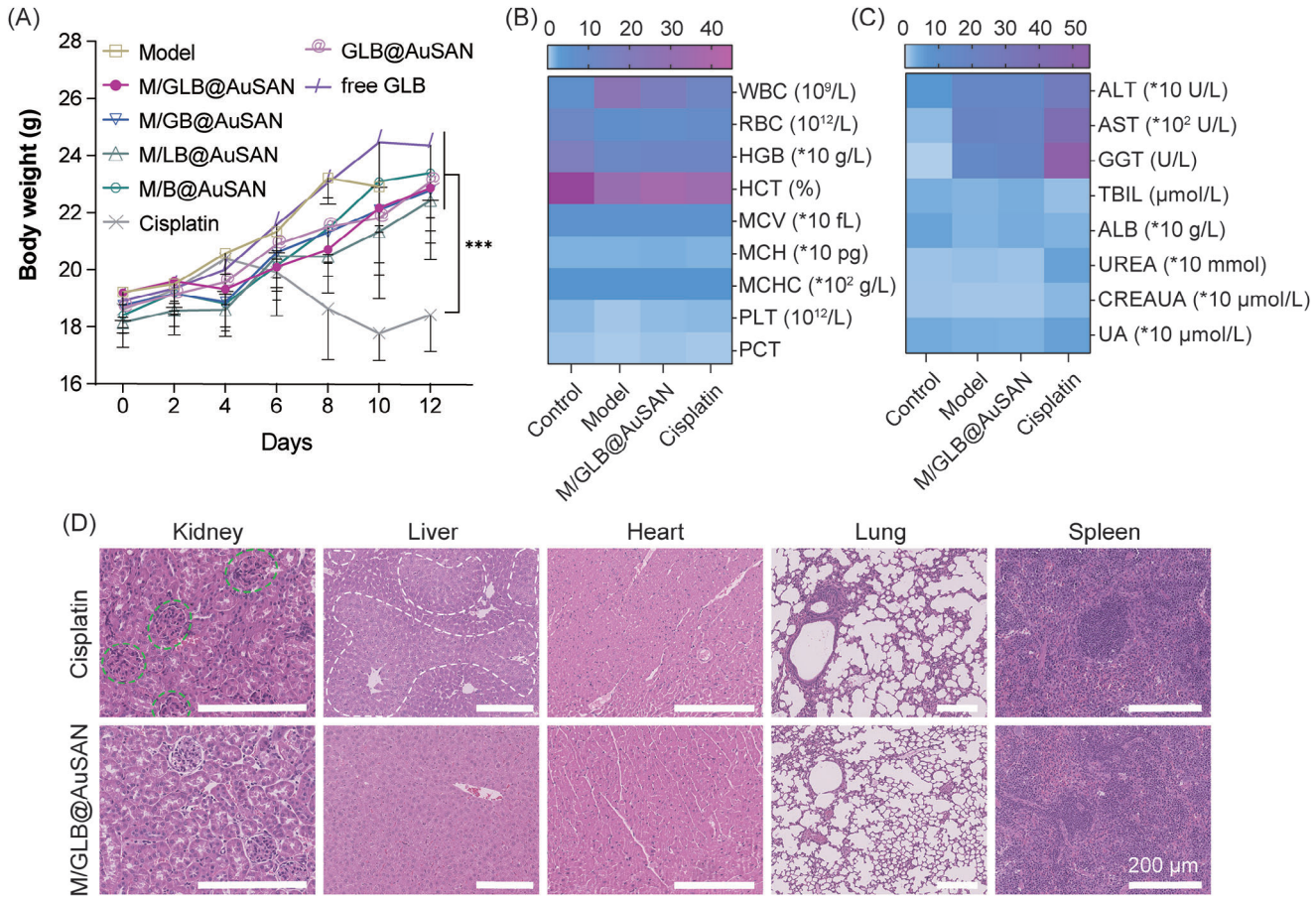

Figure 7. Biosafety of M/GLB@AuSAN. A) Body weight of mice ($n = 6$). B) Routine blood tests (The original data can be found in Figure S27, Supporting Information). C) Analysis of liver and kidney functions (The original data can be found in Figure S26, Supporting Information). D) H&E staining images of major organs from treated mice (green dotted lines: glomerular hyperproliferation; white dotted lines: liver tissue damage). The heatmap shows the mean values. ***$p \leq 0.001$.

tumors validated the occurrence of apoptosis (Figure 6H–e,f). Furthermore, apoptotic bodies containing vacuolated mitochondria (red arrows) were observed, suggesting a synergistic interaction between ferroptosis and apoptosis (Figure 6H–f). This evidence supported the hypothesis that M/GLB@AuSAN synergistically promotes tumor suppression through a cooperative mechanism involving both apoptosis and ferroptosis.

Additionally, comprehensive toxicological assessments were also carried out to ensure the safety of this therapeutic approach. After M/GLB@AuSAN treatment, no mice experienced weight loss, whereas the cisplatin group showed both deaths and weight loss (Figure S22, Supporting Information; **Figure** 7A). This indicated that M/GLB@AuSAN had superior safety over cisplatin. Three mice in the cisplatin treatment group died on the 8th and 10th day, while the survivors exhibited functional abnormalities and histological damage to the liver and kidneys, probably due to the progression of malignant tumors that increased their susceptibility to renal failure (Figures S22 and S26, Supporting Information; Figure 7D).[46] Besides, one mouse died of unknown causes in M/B@AuSAN treatment group (Figure S22, Supporting Information). Although three mice died in both the free GLB and GLB@AuSAN treatment groups, M/GLB@AuSAN avoided any mouse death. This outcome suggested that the biomimetic delivery system can enhance the biosafety of M/GLB@AuSAN, likely due to enhanced tumor penetration and retention facilitated by the cell membrane delivery mechanism.[47] It has been reported that the proliferation of malignant melanoma results in anemia, leukocytosis, thrombocytopenia, and hepatic injury.[49] Consequently, routine blood and liver function tests showed corresponding pathological changes in model mice, including erythropenia, thrombocytopenia, leukocytosis, elevated levels of aminotransferase (ALT), aspartate aminotransferase (AST), and gamma-glutamyltransferase (GGT), and a decrease in albumin (ALB) (Figure 7B,C; Figure S26, Supporting Information). However, mice treated with M/GLB@AuSAN exhibited an increase in red blood cell count, a decrease in white blood cell count, and, notably, a restoration of platelet count to healthy levels, suggesting alleviated hematological abnormalities (Figure 7B; Figure S27, Supporting Information). Hepatic and renal function tests demonstrated no additional impairment after M/GLB@AuSAN treatment (Figure 7C; Figure S26, Supporting Information). The hematoxylin and eosin (H&E) staining results further confirmed that M/GLB@AuSAN did not induce tissue damage (Figure 7D).

These findings supported M/GLB@AuSAN as a safe and effective therapeutic agent for the treatment of melanoma.

3. Conclusion

In summary, this work reports on the nanozyme/natural enzymes hybrid biomimetic M/GLB@AuSAN composite nanozyme with interconnected cascade catalysis for tumor-specific catalytic therapy. The natural enzymes loaded on the surface of nanozyme AuSAN aerobically catalyzed glucose and lactate into H_2O_2. Afterward, AuSAN timely converted H_2O_2 into ·OH, $O_2^{\bullet-}$, and O_2. In this process, generated O_2 served as positive feedback for GOx and LOx to boost their activities under aerobic conditions, thereby significantly amplifying the entire cascade catalysis for ·OH and $O_2^{\bullet-}$ generation. Additionally, B16 cell membrane coating facilitated the intracellular uptake of M/GLB@AuSAN toward homologous B16 cells to enable the effective killing of B16 cells through massive ROS while reducing toxicity to normal cells. M/GLB@AuSAN achieved sustained conversion of glucose and lactate into intracellular ROS, which enhanced mitochondrial damage, protein phosphorylation, and lipid peroxidation to boost apoptosis and ferroptosis. The robust antitumor efficacy and sustained generation of tumor ROS in vivo further substantiated that the designed M/GLB@AuSAN overcame substrate limitations in AuSAN therapy. This study developed novel Au-based SANs and offered insights into cascade catalysis design employing nanozymes.

Supporting Information

Supporting Information is available from the Wiley Online Library or from the author.

Acknowledgements

The present work was supported by the National Natural Science Foundation of China (82172591 and 81573011).

Conflict of Interest

The authors declare no conflict of interest.

Data Availability Statement

The data that support the findings of this study are available from the corresponding author upon reasonable request.

Keywords

Au single-atom nanozymes, cascade catalysis, composite nanozymes, glucose oxidase, lactate oxidase

Received: July 17, 2024
Revised: September 9, 2024
Published online:

[1] a) W. Yang, X. Yang, L. Zhu, H. Chu, X. Li, W. Xu, *Coord. Chem. Rev.* **2021**, *448*, 214170; b) H. Xiong, A. K. Datye, Y. Wang, *Adv. Mater.* **2021**, *33*, 2004319.
[2] W. Wu, L. Huang, E. Wang, S. Dong, *Chem. Sci.* **2020**, *11*, 9741.
[3] a) Q. Chen, C. Liang, X. Sun, J. Chen, Z. Yang, H. Zhao, L. Feng, Z. Liu, *Proc. Natl. Acad. Sci. USA* **2017**, *114*, 5343; b) C. M. West, F. Slevin, *Clin. Oncol.* **2019**, *31*, 595.
[4] a) D. Zhu, H. Chen, C. Huang, G. Li, X. Wang, W. Jiang, K. Fan, *Adv. Funct. Mater.* **2022**, *32*, 2110268; b) Z. Chu, J. Yang, W. Zheng, J. Sun, W. Wang, H. Qian, *Coord. Chem. Rev.* **2023**, *481*, 215049; c) F. Wei, T. W. Rees, X. Liao, L. Ji, H. Chao, *Coord. Chem. Rev.* **2021**, *432*, 213714.
[5] B. Yang, Y. Chen, J. Shi, *Adv. Mater.* **2019**, *31*, 1901778.
[6] a) E. Ricca, B. Brucher, J. H. Schrittwieser, *Adv. Synth. Catal.* **2011**, *353*, 2239; b) C. Liu, J. Xing, O. U. Akakuru, L. Luo, S. Sun, R. Zou, Z. Yu, Q. Fang, A. Wu, *Nano Lett.* **2019**, *19*, 5674.
[7] a) B. I. Reinfeld, M. Z. Madden, M. M. Wolf, A. Chytil, J. E. Bader, A. R. Patterson, A. Sugiura, A. S. Cohen, A. Ali, B. T. Do, A. Muir, C. A. Lewis, R. A. Hongo, K. L. Young, R. E. Brown, V. M. Todd, T. Huffstater, A. Abraham, R. T. O'Neil, M. H. Wilson, F. Xin, M. N. Tantawy, W. D. Merryman, R. W. Johnson, C. S. Williams, E. F. Mason, F. M. Mason, K. E. Beckermann, M. G. Vander Heiden, H. C. Manning, *Nature* **2021**, *593*, 282; b) M. G. Vander Heiden, L. C. Cantley, C. B. Thompson, *Science* **2009**, *324*, 1029.
[8] P. Singh, Y. Chen, B. Youden, D. Oakley, A. Carrier, K. Oakes, M. Servos, R. Jiang, X. Zhang, *Int. J. Pharm.* **2024**, *652*, 123814.
[9] F. Tian, S. Wang, K. Shi, X. Zhong, Y. Gu, Y. Fan, Y. Zhang, M. Yang, *Adv. Sci.* **2021**, *8*, 2102595.
[10] T. He, H. Xu, Y. Zhang, S. Yi, R. Cui, S. Xing, C. Wei, J. Lin, P. Huang, *Theranostics* **2020**, *10*, 1544.
[11] a) Z. Wang, F.-G. Wu, *Adv. Healthcare Mater.* **2022**, *11*, 2101682; b) Y. Zhu, Y. Liao, J. Zou, J. Cheng, Y. Pan, L. Lin, X. Chen, *Small* **2023**, *19*, 2300750.
[12] a) J. Wang, Y.-C. Huang, Y. Wang, H. Deng, Y. Shi, D. Wei, M. Li, C.-L. Dong, H. Jin, S. S. Mao, S. Shen, *ACS Catal.* **2023**, *13*, 2374; b) C. Peng, R. Pang, J. Li, E. Wang, *Adv. Mater.* **2023**, *36*, 2211724; c) X. Yang, A. Wang, B. Qiao, J. Li, J. Liu, T. Zhang, *Acc. Chem. Res.* **2013**, *46*, 1740.
[13] M. Zhao, N. Zhang, R. Yang, D. Chen, Y. Zhao, *Adv. Healthcare Mater.* **2021**, *10*, 2001897.
[14] S. J. Benkovic, S. Hammes, Sharon, *Science* **2003**, *301*, 1196.
[15] J. Tang, H. Shi, G. Ma, L. Luo, Z. Tang, *Front. Bioeng. Biotechnol.* **2020**, *8*, 1019.
[16] a) Z. Chen, Y. Chen, S. Chao, X. Dong, W. Chen, J. Luo, C. Liu, D. Wang, C. Chen, W. Li, J. Li, Y. Li, *ACS Catal.* **2020**, *10*, 1865; b) X. Hu, X. Chen, X. Li, C. Xu, *Adv. Funct. Mater. 34*, 2316699.
[17] N. Gong, X. Ma, X. Ye, Q. Zhou, X. Chen, X. Tan, S. Yao, S. Huo, T. Zhang, S. Chen, X. Teng, X. Hu, J. Yu, Y. Gan, H. Jiang, J. Li, X.-J. Liang, *Nat. Nanotechnol.* **2019**, *14*, 379.
[18] a) W. He, J. Wu, J. Liu, J. Li, *Adv. Funct. Mater.* **2024**, *34*, 2312116; b) C. Peng, R. Pang, J. Li, E. Wang, *Adv. Mater.* **2024**, *36*, 2211724.
[19] a) J. Li, Z. Yang, Y. Li, G. Zhang, *J. Hazard. Mater.* **2022**, *429*, 128285; b) Y. Chen, S. Ji, C. Chen, Q. Peng, D. Wang, Y. Li, *Joule* **2018**, *2*, 1242.
[20] a) P. Amin, A. Shojaei, T. Hamzehlouyan, *Microporous Mesoporous Mater.* **2022**, *343*, 112149; b) J. Qiao, W. Ma, X. Du, X. Ma, Z. Liu, J. Li, G. Guan, A. Abudula, X. Hao, *Sep. Purif. Technol.* **2022**, *295*, 121222; c) T. Ueda, T. Yamatani, M. Okumura, *J. Phys. Chem. C* **2019**, *123*, 27542.
[21] M. Zhao, R. Yang, Y. Wei, J. Su, X. Wang, N. Zhang, P. Sun, D. Chen, Y. Zhao, *Nano Today* **2022**, *44*, 101493.
[22] W. Yu, H. Huang, Y. Qin, D. Zhang, Y. Zhang, K. Liu, Y. Zhang, J. Lai, L. Wang, *Adv. Energy Mater.* **2022**, *12*, 2200110.
[23] a) Y. Gao, T. Li, Y. Zhu, Z. Chen, J. Liang, Q. Zeng, L. Lyu, C. Hu, *J. Hazard. Mater.* **2020**, *393*, 121280; b) Y. Feng, C. Wang, F. Ke, J. Zang, J. Zhu, *Nanomaterials* **2018**, *8*, 446.

[24] H. Zhang, S. Hwang, M. Wang, Z. Feng, S. Karakalos, L. Luo, Z. Qiao, X. Xie, C. Wang, D. Su, Y. Shao, G. Wu, *J. Am. Chem. Soc.* **2017**, *139*, 14143.
[25] Y. Jia, L. Zhang, L. Zhuang, H. Liu, X. Yan, X. Wang, J. Liu, J. Wang, Y. Zheng, Z. Xiao, E. Taran, J. Chen, D. Yang, Z. Zhu, S. Wang, L. Dai, X. Yao, *Nat. Catal.* **2019**, *2*, 688.
[26] Y. Peng, B. Lu, S. Chen, *Adv. Mater.* **2018**, *30*, 1801995.
[27] Z. Song, J. Li, K. D. Davis, X. Li, J. Zhang, L. Zhang, X. Sun, *Small Methods* **2022**, *6*, 2201078.
[28] T. Matsuyama, J. Hirayama, Y. Fujiki, S. Kikkawa, W. Kurashige, H. Asakura, N. Kawamura, Y. Negishi, N. Nakatani, K. Hatada, F. Ota, S. Yamazoe, *J. Phys. Chem. C* **2021**, *125*, 3143.
[29] a) Z. D. An, P. P. Yang, D. L. Duan, J. Li, T. Wan, Y. Kong, S. Caratzoulas, S. T. Xiang, J. X. Liu, L. Huang, A. I. Frenkel, Y. Y. Jiang, R. Long, Z. X. Li, D. G. Vlachos, *Nat. Commun.* **2023**, *14*, 6666; b) C. C. Hou, L. L. Zou, L. M. Sun, K. X. Zhang, Z. Liu, Y. W. Li, C. X. Li, R. Q. Zou, J. H. Yu, Q. Xu, *Angew. Chem. Int. Ed.* **2020**, *59*, 7384; c) Z. Li, B. Ding, J. Li, H. Chen, J. Zhang, J. Tan, X. Ma, D. Han, P. a. Ma, J. Lin, *Angew. Chem. Int. Ed.* **2024**, https://doi.org/10.1002/anie.202413661.
[30] M. Huang, R. Ding, J. Yang, W. Shi, S. Shi, L. Chen, S. Liu, X. Yin, *J. Electrochem. Soc.* **2022**, *169*, 106507.
[31] S. Reuter, S. C. Gupta, M. M. Chaturvedi, B. B. Aggarwal, *Free Radic. Biol. Med.* **2010**, *49*, 1603.
[32] Z. Dong, L. Feng, Y. Hao, Q. Li, M. Chen, Z. Yang, H. Zhao, Z. Liu, *Chem* **2020**, *6*, 1391.
[33] S. Li, Z. Zhuang, T. Wu, J.-C. Lin, Z.-X. Liu, L.-F. Zhou, T. Dai, L. Lu, H.-Q. Ju, *Redox Biol.* **2018**, *18*, 246.
[34] S. Liu, Z. Li, C. Wang, W. Tao, M. Huang, M. Zuo, Y. Yang, K. Yang, L. Zhang, S. Chen, P. Xu, Q. Chen, *Nat. Commun.* **2020**, *11*, 938.
[35] O. Cantoni, G. Brandi, L. Salvaggio, F. Cattabeni, *Ann. Ist. Super. Sanita* **1989**, *25*, 69.
[36] Y. Xiao, P. Chen, S. Lei, F. Bai, L. Fu, J. Lin, P. Huang, *Angew. Chem., Int. Ed.* **2022**, *61*, 202204584.
[37] a) R. Li, Y. He, S. Zhang, J. Qin, J. Wang, *Acta Pharm. Sin. B* **2018**, *8*, 14; b) L. Chen, W. Hong, W. Ren, T. Xu, Z. Qian, Z. He, *Signal Transduction Targeted Ther.* **2021**, *6*, 225.
[38] X. Guo, D. Lu, D. Zhang, J. Deng, X. Zhang, Z. Wang, L. Xiao, Y. Zhao, *Mater. Sci. Eng., C* **2020**, *106*, 110227.
[39] a) P. Singh, Y. L. Chen, B. Youden, D. Oakley, A. Carrier, K. Oakes, M. Servos, R. Q. Jiang, X. Zhang, *Int. J. Pharm.* **2024**, *652*; b) X. Y. Zhu, J. B. Wu, R. X. Liu, H. D. Xiang, W. Q. Zhang, Q. C. Chang, S. S. Wang, R. Jiang, F. Zhao, Q. Q. Li, L. Huang, L. Yan, Y. L. Zhao, *ACS Nano* **2022**, *16*, 18849; c) F. Tian, S. Y. Wang, K. D. Shi, X. J. Zhong, Y. T. Gu, Y. D. Fan, Y. Zhang, M. Yang, *Adv. Sci.* **2021**, *8*, 2102595.
[40] a) Y. P. Xiao, P. H. Chen, S. Lei, F. Bai, L. H. Fu, J. Lin, P. Huang, *Angew. Chem. Int. Ed.* **2022**, *61*, 202204584; b) T. He, H. Xu, Y. F. Zhang, S. J. Yi, R. Cui, S. J. Xing, C. L. Wei, J. Lin, P. Huang, *Theranostics* **2020**, *10*, 1544.
[41] a) L. Rochette, G. Dogon, E. Rigal, M. Zeller, Y. Cottin, C. Vergely, *Int. J. Mol. Sci.* **2023**, *24*, 449; b) G. Filomeni, D. De Zio, F. Cecconi, *Cell Death Differ.* **2015**, *22*, 377; c) J. Zhang, X. Wang, V. Vikash, Q. Ye, D. Wu, Y. Liu, W. Dong, *Oxidative Med. Cell. Longev.* **2016**, *2016*, 4350965.
[42] a) N. A. Graham, M. Tahmasian, B. Kohli, E. Komisopoulou, M. Zhu, I. Vivanco, M. A. Teitell, H. Wu, A. Ribas, R. S. Lo, I. K. Mellinghoff, P. S. Mischel, T. G. Graeber, *Mol. Syst. Biol.* **2012**, *8*, 589; b) G. K. Raut, M. Chakrabarti, D. Pamarthy, M. P. Bhadra, *Free Radic. Biol. Med.* **2019**, *145*, 428; c) K. Miki, M. Yagi, D. Kang, Y. Kunisaki, K. Yoshimoto, T. Uchiumi, *iScience* **2024**, *27*; d) K. Miki, M. Yagi, K. Yoshimoto, D. Kang, T. Uchiumi, *Oncogenesis* **2022**, *11*, 59.
[43] D. Sergi, N. Luscombe-Marsh, N. Naumovski, M. Abeywardena, N. O'Callaghan, *Front. Nutr.* **2021**, *8*, 663838.
[44] D. Spierings, G. McStay, M. Saleh, C. Bender, J. Chipuk, U. Maurer, D. R. Green, *Science* **2005**, *310*, 66.
[45] M. Gao, J. Yi, J. Zhu, A. M. Minikes, P. Monian, C. B. Thompson, X. Jiang, *Mol. Cell* **2019**, *73*, 354.
[46] Y. Shimeda, Y. Hirotani, Y. Akimoto, K. Shindou, Y. Ijiri, T. Nishihori, K. Tanaka, *Biol. Pharm. Bull.* **2005**, *28*, 1635.
[47] a) J. Hu, X. Yuan, F. Wang, H. Gao, X. Liu, W. Zhang, *Chin. Chem. Lett.* **2021**, *32*, 1341; b) B. Zheng, Z. Liu, H. Wang, L. Sun, W.-F. Lai, H. Zhang, J. Wang, Y. Liu, X. Qin, X. Qi, S. Wang, Y. Shen, P. Zhang, D. Zhang, *J. Controlled Release* **2022**, *351*, 834.
[48] J. J. Lemasters, *Redox Biol.* **2014**, *2*, 749.
[49] a) J. Cho, G. Saffouri, T. Smyrk, T. Viggiano, *Am. J. Gastroenterol.* **2016**, *111*, S1374; b) K. H. Kim, N. S. Sim, J. S. Chang, Y. B. Kim, *Cancer Immunol., Immunother.* **2020**, *69*, 1265; c) S. G. Pascal, A. M. Saulenas, G. A. Fournier, J. M. Seddon, R. M. Hatfield, D. M. Albert, *Am. J. Ophthalmol.* **1985**, *100*, 448.